3D printing of crack-free high strength Zr-based bulk metallic glass composite by selective laser melting

CrossMark

Di Ouyang, Ning Li[**], Wei Xing, Jianji Zhang, Lin Liu[*]

State Key Lab for Materials Processing and Die & Mold Technology, School of Materials Science and Engineering, Huazhong University of Science and Technology, Wuhan 430074, PR China

ARTICLE INFO

ABSTRACT

3D printing of crack-free bulk metallic glasses remains challenge due to the generation of huge thermal stress during the selective laser melting and their intrinsic brittleness. Herein, $Zr_{55}Cu_{30}Ni_5Al_{10}$ system was selected and 3D printed by selective laser melting technique. The results indicated that bulk metallic glassy composite comprises a large fraction (about 83%) of amorphous phase and minor fraction of intermetallic compounds with free of cracks were successfully fabricated. The 3D printed metallic glassy composite exhibited high strength over 1500 MPa. Experiment combined with finite-element-method simulation not only revealed the mechanism of crystallization at heat affected zones, but demonstrated that low thermal stress reduce the risk of micro-cracks generation and fracture toughness plays a crucial role in suppression the crack propagation during selective laser melting process.

1. Introduction

Efforts have been devoted to manufacturing of bulk metallic glasses (BMGs) in the past decade due to their processing limitation at ambient temperature. Though copper mold casting method has been used to fabricate simple components, but the complexity and dimension are intrinsically restrained owing to the requirement of high cooling rate [1,2]. Thermoplastic forming (TPF) that benefits from the superplasticity of supercooled BMGs, have been widely employed to fabricate precise and versatile geometries on length scales ranging from 10 nm to several centimeters [3–12], exhibiting potential applications in the miniaturization of modern industry. Whereas the fabrication of complicated 3D structures still remains challenge due to high viscosity of the supercooled liquids of BMGs and conspicuous interfacial effect between materials and mold [3,13]. By comparison with copper mold casting and TPF, selective laser melting (SLM) is a promising additive manufacture technique with advantages of direct fabrication of 3D parts with complex geometries. During SLM, components are manufactured by selective melting and consolidation of thin layers of powders using a scanning laser beam according to CAD designed data of the components [14]. Since only small volumes of material are molten and cooled as the laser beam scans across the powder bed during SLM [15], the cooling rates reach up to 10^4–10^6K/s [16–18] that is higher than the critical cooling rate required for most of BMG systems (10^2–10^4 K/s)

[19–21].

In 2013, Pauly et al. [22] first reported the 3D printed scaffold structure by selective laser melting of Fe-based amorphous powders, and found that the amorphous structure could be retained under appropriate conditions [23]. The 3D printing of BMGs was then patented by Apple Ico., for seeking applications in the key components of consumer electronics [24]. Recently, Li et al. [25,26] revealed that the inhomogeneous energy density during SLM induces heterogeneous distribution of microstructure and mechanical properties. Notable that the rapid heating/cooling during SLM usually generate a steep temperature gradient, inducing a huge thermal stress and causing micro-cracks in the 3D printed parts [27]. To alleviate the micro-crack phenomenon, a re-scanning strategy was applied in an Al-based bulk metallic glass composite (BMGC) during SLM [26]. Li et al. [28] also found that the micro-crack can avoided in a Zr-based BMG fabricated by SLM. The question then arises as what are the decisive parameters to hinder micro-cracking of BMGs prepared by SLM, this is crucial to the properties and applications of 3D printed BMGs compounds. It is well accepted that the materials with high fracture toughness essentially performs a good ability of preventing crack propagation, due to the plastic deformation that dissipates fracture energy, moderates stress concentration in front of crack tip and shield the crack propagation. Previous work [15,29,30] has also revealed that micro-cracks usually happened in alloys with low fracture toughness. Accordingly, we

---

* Corresponding author.
** Corresponding author.
   E-mail addresses: hslining@mail.hust.edu.cn (N. Li), lliu2000@mail.hust.edu.cn (L. Liu).
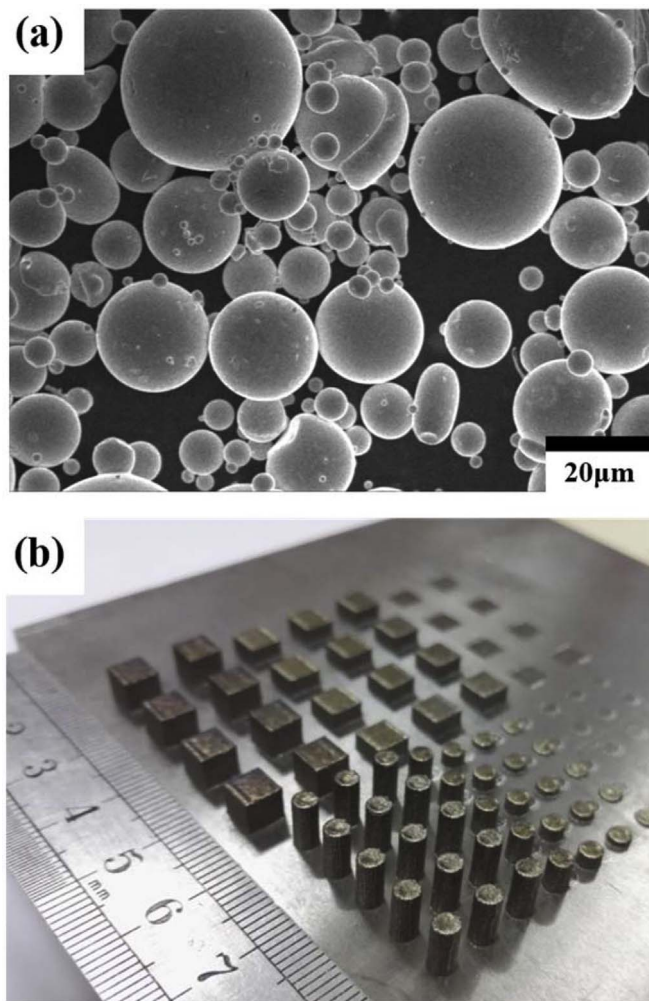
Fig. 1. (a) SEM micrographs of gas-atomized Zr-based amorphous alloy powder, (b) 3D printed Zr-based BMG samples.

selected $Zr_{55}Cu_{30}Ni_5Al_{10}$ metallic glass alloy with fracture toughness of 70 MPa m$^{1/2}$ [31] in this research, and 3D printed by selective laser melting. The results reveal that a crack-free Zr-based bulk metallic glassy composite with high strength could be fabricated. The physical origin of the above scenario can be fundamentally understood on the basis of low thermal stress that reduce the risk of micro-cracks generation, and high fracture toughness plays a crucial role in suppression the crack propagation during selective laser melting process.

2. Materials and methods

The $Zr_{55}Cu_{30}Ni_5Al_{10}$ (in at.%) amorphous powders were produced through high-pressure inert gas atomization, the particles used for SLM have smooth surface and size ranges from 2 μm to 33 μm, as illustrated in Fig. 1(a). The SLM experiment was performed by commercial SLM machine (FORWEDO LM-120, Forwedo), equipped with a Nd:YAG fiber laser (maximum power, P_{max} = 500 W, wavelength λ = 1060 nm, focus diameter d = 80 μm) and an F-theta lens systems. The forming chamber was vacuumed and protected by argon gas with the oxygen content below 100 ppm. Here, P = 240 W, scanning speed V = 1200 mm/s, powder bed layer thickness h = 60 μm, scan line hatch spacing t = 100 μm, and scanning direction of 90° alternately among layers were adopted in this work based on experienced experiments. The cylindrical specimens with diameter of 3 mm and height of 7.2 mm were 3D-printed, as shown in Fig. 1(b). For comparison, rods with a diameter of 3 mm and a length of 90 mm, were fabricated by arc-
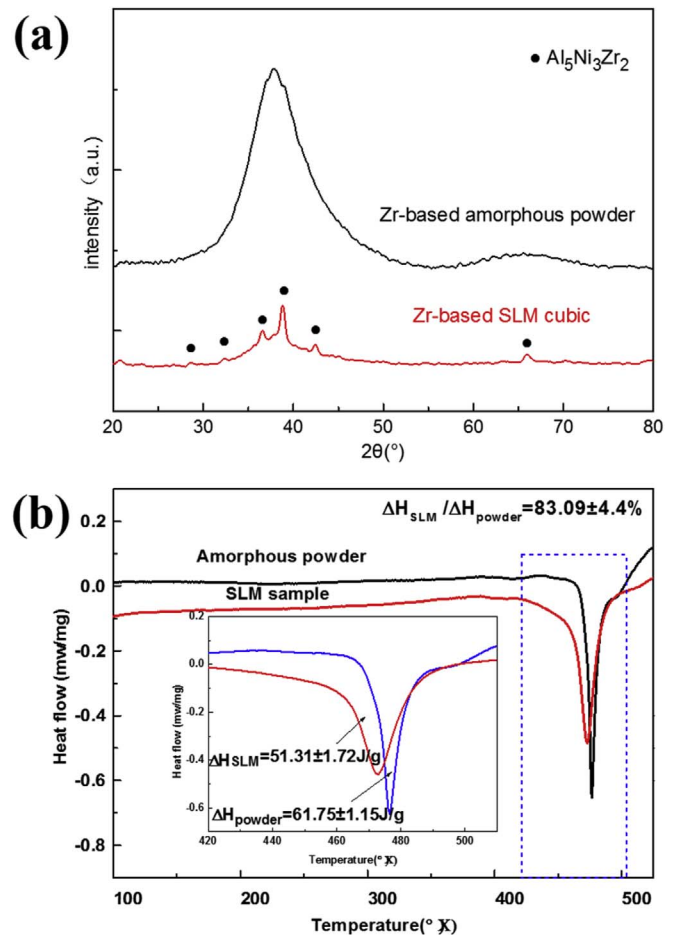

Fig. 2. (a) and (b) exhibit the corresponding X-ray patterns and DSC curves, respectively, as compared with the original powder.

melting amorphous powder under a Ti-gettered argon atmosphere, followed by suck casting into copper molds.

To detect the laser induced microstructural evolution, the 3D printed rod samples were analyzed by X-ray diffraction (XRD, 7000SX, Shimadzu) and differential scanning calorimetry (DSC, NETZSCH STA 449F3). The microstructure around the molten pool was characterized through transmission electron microscopy (TEM, FEI Tecnai G20, 200 kV). The TEM thin foil was prepared by focused ion beam (FIB, Quanta 3D FEG). The mechanical properties of the 3D printed Zr-based alloy rods were tested under quasi-static uniaxial compression (strain rate of 1 × 10^{-4} s^{-1}) using a Zwick machine (Zwick/Roell 020) at room temperature. The micrographs of the samples' cross section were observed through an optical microscopy (Leica DFC450) after being polished and etched with a corrosive agent (mixture of 15 ml H_2O, 15 ml HNO_3 and 1.5 ml HF). The fractural surfaces were characterized by scanning electron microscopy (SEM, QUANTA FEG450). To probe the fraction and distribution of porosity formed during SLM, the printed specimen with diameter of 3 mm and height of 7.2 mm was tested by lab-based high resolution X-ray tomography (XRT) [32,33]. Wherein X-rays are transmitted through sample and are detected using a scintillator screen, the raw tomographic data were then imported to tomographic reconstruction software, using inverse Fourier transforms to create three-dimensional image, the XRT investigations were performed with a voxel size of (1.36 μm^3).
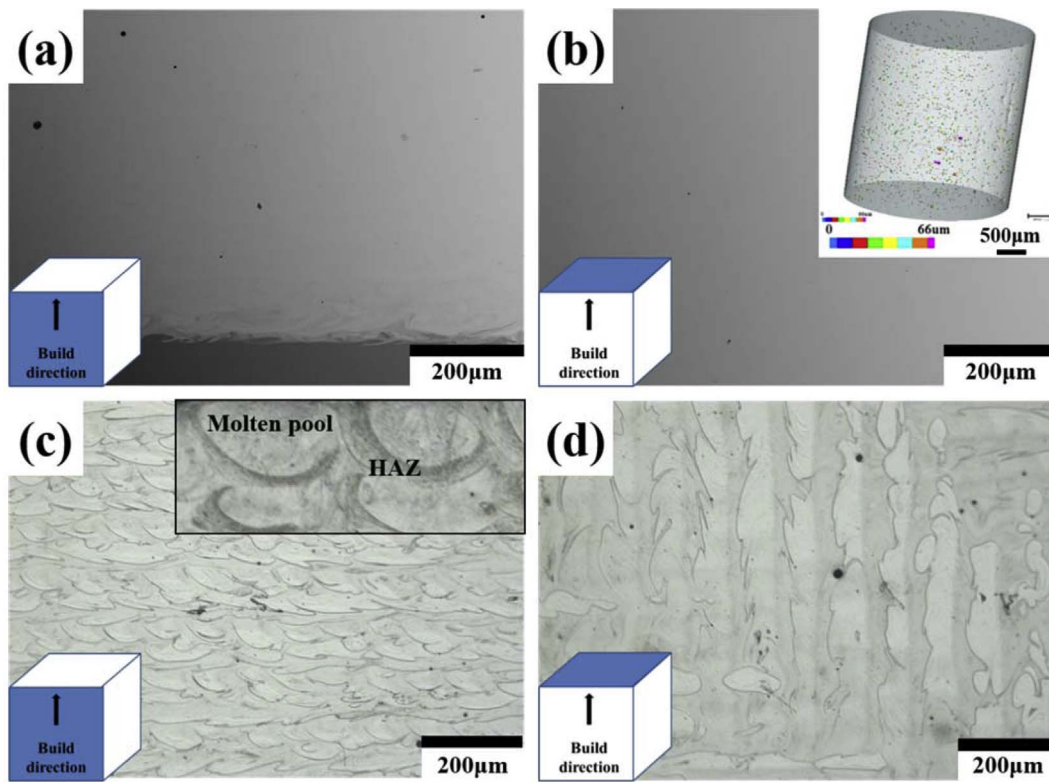
Fig. 3. (a–b) Side and top view of SEM-BSE micrographs of 3D printed Zr-based BMG, respectively, the inset image in (b) shows the distribution of pores; (c–d) Side and top view of 3D printed Zr-based BMG after etching by the corrode, respectively, the inset image show the molten pool and HAZ.
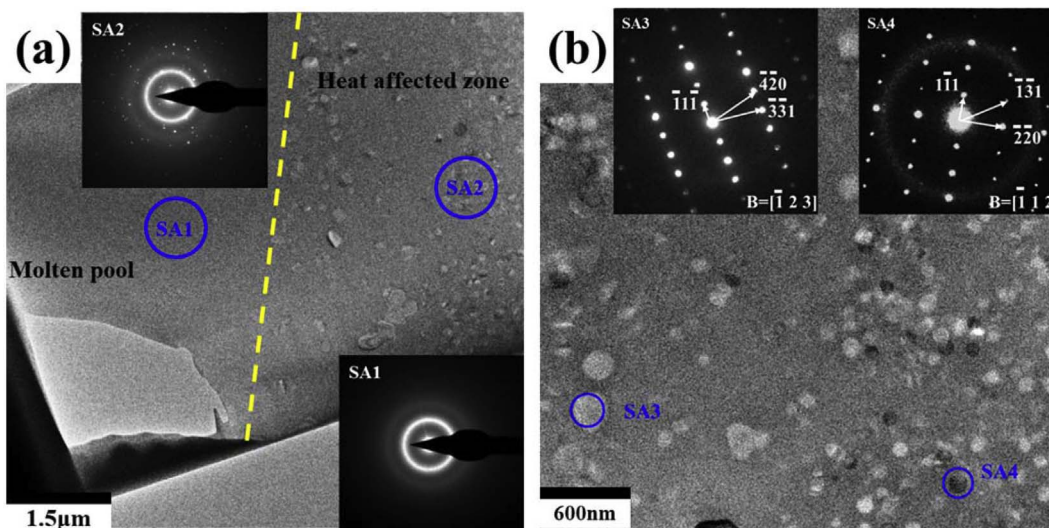

Fig. 4. (a) TEM bright-field image shows the boundary of molten pool and heat affected zone of Fig. 2(c), (b) diffraction patterns for selected positions in heat affected zone, the nano-crystallines are $Al_5Ni_3Zr_2$ (SA3) and $NiZr_2$ (SA4).

3. Results

3.1. Microstructure and defects

Fig. 2(a) shows the X-ray diffraction pattern of the 3D printed Zr-based alloy cylinders, which was compared with the original powders that exhibits only broad diffraction (*i.e.* fully amorphous structure). While for the 3D printed parts, some weak Bragg peaks (corresponding to $Al_5Ni_3Zr_2$ phase) are superimposed on a broad spectrum, indicating the occurrence of partial crystallization during the SLM process. The low intensities of peaks reveals low fraction of crystallized phase, which was further demonstrated by DSC, as depicted in Fig. 2(b). From which

83 ± 4.4 vol% amorphous phase in the 3D printed Zr-based BMG composite was calculated by comparing the crystallization enthalpy with that of fully amorphous powders.

Fig. 3(a) and (b) show the side and top view of SEM micrographs of the 3D printed Zr-based BMG composite, respectively, wherein no cracks were observed. While some tiny pores was probed through lab-based high resolution X-ray tomography (XRT), as shown in the insert of Fig. 3(b). Which reveals volume fraction of about $0.12 \pm 0.01\%$ pores dispersed randomly in the 3D printed sample, indicating that 3D printed parts are almost fully densified. To further measure the real porosity, additional density measurements based on the Archimedean principle was performed. The result has shown that density of 3D
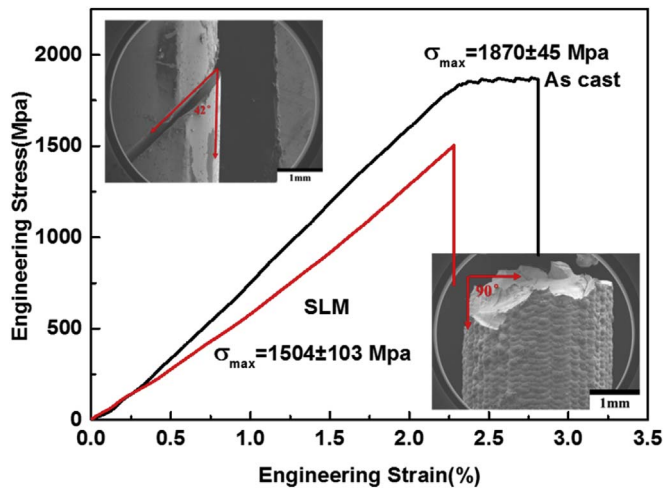
Fig. 5. Compressive stress-strain curves of the 3D printed Zr-based BMG rods, as compared with the as-cast one.

printed sample is 6.83213 g/cm³, by comparing the density of casting sample (6.83966 g/cm³), the relative density of 3D printed sample is 99.89%, which is almost in consistent with the results of XRT. In addition, the scanning track including molten pools and heat affected zones (HAZ) can be clearly observed, as illustrated in Fig. 3(c) and (d).

To detect the possible microstructural evolution around molten pool during the process of SLM, a small area including molten pool and heat affected zone (HAZ) was extracted via FIB and examined by TEM, and the results are illustrated in Fig. 4(a) and (b). The selected area electron diffraction (SAD) indicated that the region in the molten pool (labeled by SA1) is fully amorphous, while the region in the heat affected zone (labeled by SA2) contains mixing structure of amorphous phase and some nanocrystals with dimensions of 100–200 nm (Fig. 4(b)). Nano-beam diffraction revealed that the crystals formed in HAZ are mainly $Al_5Ni_3Zr_2$ (FCC structure) and $NiZr_2$ (FCC structure) intermetallic compounds, which is in consistent with the XRD result.

3.2. Mechanical properties

Fig. 5 exhibits the quasi-static uniaxial compressive stress-strain curves of the 3D printed Zr-based BMGC rods with diameter of 3 mm and height of 6 mm, and compared with the as-cast one. The as-cast BMG possesses yield strength of 1870 ± 45 MPa and plastic strain of 0.5%, consistent with the data in literature [34]. Though the 3D printed Zr-based BMGC cylinders exhibit little plasticity, the sample still remains sufficient high yield strength of about 1504 ± 103 MPa. It is also notes that the 3D printed parts exhibit a lower value of Young's modulus than that of the cast sample as shown in Fig. 5, mainly due to the defects formed in the 3D printed parts. In addition, the fractural angle is about 90°, different absolutely with the typical as-cast BMGs (about 42°), probably due to the layered structure as well as brittle crystallized phases dispersed in HAZ in the 3D printed BMG composite.

Fig. 6(a)–(c) show the fracture surface of the 3D printed sample, two main regions, *i.e.* "A" and "B" are selected and observed by SEM. From zone A as depicted in Fig. 6(b), vein-like patterns (identical to the fractural features of the pure Zr-based BMG [35]) and smooth fractural features (caused by the brittle nanocrystals) are clearly observed, demonstrating again the composite structure of the 3D printed alloys. The typical vein-like patterns indicating the occurrence of local viscous flow of metallic glass by adiabatic shearing during fracture, which are also detected in Zone B, as shown in Fig. 6(c).

4. Discussion

4.1. Crystallization at heat affected zone

The above results have revealed that partial crystallization occurred at heat affected zones around the molten pools, as reported by other literature [36]. The brittle nanocrystals at heat affected zone is destructive to the mechanical properties of the 3D printed Zr-based metallic glass composite, such as little plasticity as shown in Fig. 5. In general, crystallization is essentially related to the temperature history of material during the process of selective laser melting. To detect this information and understand the effect of temperature distribution on crystallization, finite element method (FEM) was introduced. The FEM Simulations were performed using the commercial ABAQUS software
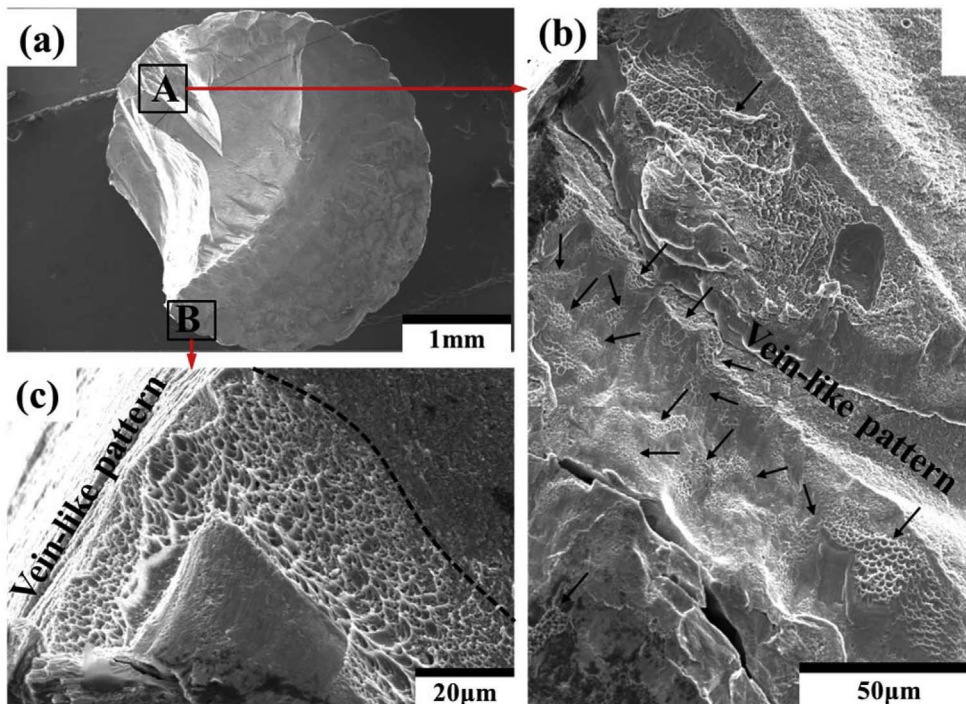

Fig. 6. (a) Compressive stress-strain curves of the 3D printed Zr-based BMG rods, as compared with the as-cast one. (b) Macroscopic morphology of the fracture surface of 3D printed Zr-BMG cylinder, (c–d) different regions reveal brittle and vein-like features.

Table 1
Parameters used for finite element simulation.

Parameter	Value
Laser power, P (W)	240
Total laser beam radius, d (mm)	0.08
Laser energy absorptivity, A	0.04
Scanning speed, V (m/s)	1.2
Density of Zr-based MG powder, ρ (kg m^{-3})	4129.8
Coefficient for the heat convection, h (W m^{-2} K^{-1})	20
The Stefan-Boltzmann constant, δ(W m^{-2} K^{-4})	5.67×10^{-8}
Radiation emissivity, ε	0.3

Table 2
Thermal physical parameters of solid 3D printed Zr-based MG.

Temperature, T (°C)	20	100	200	300	400	500	600	700	800
Thermal conductivity, k (W/m°C)	4.9	6.2	7.4	6.8	6.6	7.6	7.7	10.1	9.6
Heat capacity,c (J/ kg°C)	326	346	342	271	233	−323	0.112	362	375

by using a moving heat source which obeys Gaussian distribution [37]. Parameters used for finite element simulation are listed in Tables 1 and 2. Fig. 7(a) and (b) exhibit the top and side views of simulated instantaneous temperature field around molten pool, the dimension of it is 115 μm height and 150 width. It can be seen that the highest temperature of 2200 °C could be reached at the center of molten pool during SLM process, which is much higher than the melting

temperature of 892 °C (as signed at the molten boundary) of the alloy system. The temperature drops down quickly when going away from molten pool, leading to the formation of a steep temperature gradient around the molten pool.

To clarify the effect of temperature histories on crystallization, three typical positions signed Sa (located in molten pool close to the molten pool boundary), Sb (located at HAZ) and Sc (beyond HAZ) were selected (as described in Fig. 7(b)). Putting the variable of time in FEM simulation, the corresponding heating-cooling curves at above three positions were obtained, as depicted in Fig. 7(c), from which cooling rate at the positions of Sa, Sb and Sc was calculated to be 8.2×10^4 °C/ s, 4.5×10^4 °C/s, 1.1×10^4 °C/s, respectively. Noted that the critical cooling rate required for the formation of amorphous phase in $Zr_{55}Cu_{30}Ni_5Al_{10}$ system is about 10 °C/s [39], the high cooling rate ensures the formation of fully amorphous structure in molten pools during the SLM process, which is consistent with the TEM results. Although the cooling rate in HAZ is also high enough, the heat affected zone (HAZ) in glass state, in this case, happening of crystallization is not determined by cooling rate but by temperature increase. If the temperature is higher than T_x, crystallization is hard to hamper and cannot be understood according to the critical cooling rate.

In addition, the FEM simulation also revealed that the reheating at heat affected zone last only about 5 ms during laser scanning, which results in the formation of nanocrystals due to lacking time to grow, that is why HAZ usually has a composite structure mixed with amorphous phase and some nanocrystals, as displays in Fig. 4(b).
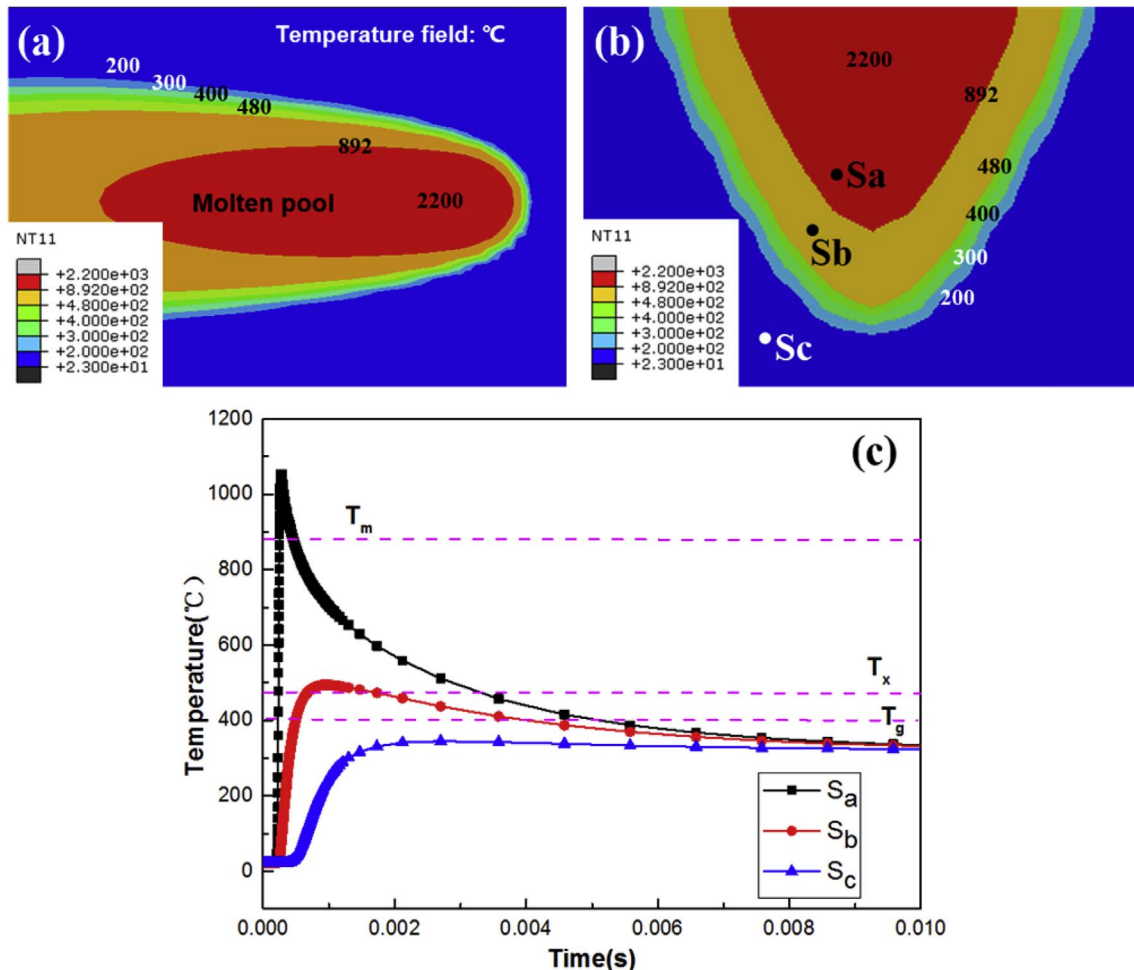

Fig. 7. (a–b) FEM simulated temperature field of top view and side view respectively; (c) Heating cooling curves in the molten pool (Sa), HAZ (Sb) and un-affected zone (Sc) from (b).
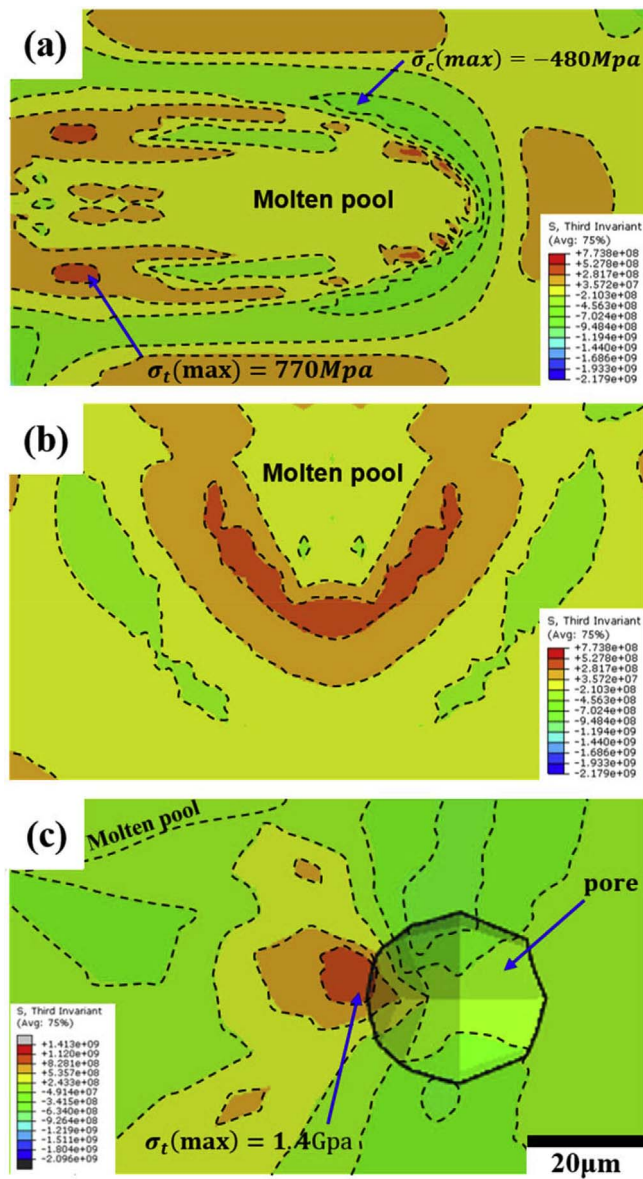
Fig. 8. (a–b) FEM simulated thermal stress field around molten pool of side view and top view respectively; (c) Stress concentration occurs in the pore near the molten pool.

4.2. Free of micro-crack

In general, the rapid heating and cooling during SLM process could generate steep temperature gradient and induce huge thermal stress [38], causing formation of micro-cracks in the 3D printing parts [21,24]. On the basis of the FEM simulation, the thermal stress induced by temperature gradient in the $Zr_{55}Cu_{30}Ni_5Al_{10}$ bulk metallic glass during the process of SLM was also obtained. Fig. 8(a) and (b) exhibit the inhomogeneous thermal stress field from top and side view, respectively, wherein compressive stress with a maximum value (σ_{c-max}) of 480 MPa generated in front and at side of the molten pool due to the expansion of material affected by high temperature. While along the track of the scanning, tensile stress (σ_{t-max} = 770 MPa) created somewhere behind the molten pool owing to the contraction induced by liquid to solid transition, both are much smaller than the fractural strength (1504 MPa) of the $Zr_{55}Cu_{30}Ni_5Al_{10}$ BMG (Fig. 5). In this case, micro-cracks are hardly generated in the 3D printed $Zr_{55}Cu_{30}Ni_5Al_{10}$ BMG.

However, defects such as pores always formed in the 3D printed component according to previous literature [40]. In this work, we probe the defects through lab-based high resolution 3D X-ray tomography (XRT), and find some tiny pores with average size of about 30 μm and volume fraction of about 0.12% dispersed randomly in the 3D printed sample (in the insert in Fig. 3(b)). Based on the tomography from XRT, the pores in the 3D-printed BMGs have commonly spherical shape, so we use spherical pore to calculate the stress concentration on the basis of FEM simulation. The simulation results have shown that the stress concentration around defects (pores) could reach up to about 1.4 Gpa at the boundary of spherical pore with average diameter 30 μm, which can easily trigger the initiation of micro-cracks. Nevertheless, micro-cracks are hardly observed in the printed $Zr_{55}Cu_{30}Ni_5Al_{10}$ BMG, similar to other alloys such as Ti_6Al_4V [14], SS316L [41] and Inconel 718 [42] alloys.

The physical origin for the above scenario can be understood fundamentally on the basis of fracture mechanisms of materials, wherein the fracture toughness play a crucial role in hindering micro-crack propagation. If the localized stress near the crack tip is larger than the yield stress (σ_{ys}) of the alloys due to the elastic energy absorption of material in loading, plastic deformation would occur. While for those alloys with low fracture toughness, such as $Fe_{41}Co_7Cr_{15}Mo_{14}C_{15}B_6Y_2$, the plastic deformation zone is very small, therefore the release of elastic energy through plastic deformation is limited. In such a case, the accumulated plastic energy and the stress would be very high. Once the stress is over the fracture stress, the crack can no longer be constrained, crack propagation initiates and global failure occurs, that is why micro-crack always happens in Fe-based BMGs with small fracture toughness during SLM [22]. On the contrary, the high fracture toughness indicates the formation of large plastic zone that dissipates much fracture energy, which moderates the stress concentration in front of crack tip and shield the crack initiation or crack propagation [43], leading to the formation of crack-free BMG composite as observed in this work.

5. Conclusions

The crack-free Zr-based bulk metallic glass composite exhibited high strength over 1500 Mpa was successfully fabricated by 3D printing technique of selective laser melting and analyzed by experiments as well as Finite Element Method, the main results are summarized as follows:

(1) The 3D printed BMG composite, composed of 83 vol% fraction of amorphous phase was obtained, Fully amorphous structure was formed in the molten pools, while partial crystallization occurred in the heat affected zone where the reheating temperature is over crystallization temperature.
(2) Finite Element Method reveals that the formation of crack-free BMG composite in the present Zr-based system is attributed to a low thermal stress generated in the selective laser melting process. In addition, the high toughness of the Zr-based BMG system could also pay a role in suppression of micro-crack formation.

Acknowledgements

References

[1] V. Keppens, Z. Zhang, O.N. Senkov, D.B. Miracle, Localized Einstein modes in Ca-based bulk metallic glasses, Philos. Mag. 87 (2007) 503–508.
[2] J. Schroers, Bulk metallic glasses, Phys. Today 66 (2013) 32–37.
[3] N. Li, D.J. Li, L. Liu, Correlation between flow characteristics and interfacial friction

behaviour of a Zr-based metallic glass during micro-extrusion, Philos. Mag. 93 (2013) 1859–1872.

[4] G. Kumar, A. Desai, J. Schroers, Bulk metallic glass: the smaller the better, Adv. Mater. 23 (2011) 461–476.

[5] N. Li, Y. Chen, M.Q. Jiang, D.J. Li, J.J. He, Y. Wu, L. Liu, A thermoplastic forming map of a Zr-based bulk metallic glass, Acta Mater. 61 (2013) 1921–1931.

[6] N. Li, X.N. Xu, Z.Z. Zheng, L. Liu, Enhanced formability of a Zr-based bulk metallic glass in a supercooled liquid state by vibrational loading, Acta Mater. 65 (2014) 400–411.

[7] T. Xia, N. Li, Y. Wu, L. Liu, Patterned superhydrophobic surface based on Pd-based metallic glass, Appl. Phys. Lett. 101 (2012) 081601.

[8] W. Chen, Z. Liu, H.M. Robinson, J. Schroers, Flaw tolerance vs. performance: a tradeoff in metallic glass cellular structures, Acta Mater. 73 (2014) 259–274.

[9] G. Kumar, H.X. Tang, J. Schroers, Nanomoulding with amorphous metals, Nature 457 (2009) 868–872.

[10] J.J. He, N. Li, N. Tang, X.Y. Wang, C. Zhang, L. Liu, The precision replication of a microchannel mould by hot-embossing a Zr-based bulk metallic glass, Intermetallics 21 (2012) 50–55.

[11] N. Li, T. Xia, L. Heng, L. Liu, Superhydrophobic Zr-based metallic glass surface with high adhesive force, Appl. Phys. Lett. 102 (2013) 251603.

[12] M. Hasan, G. Kumar, High-throughput drawing and testing of metallic glass nanostructures, Nanoscale 9 (2017) 3261–3268.

[13] N. Li, W. Chen, L. Liu, Thermoplastic micro-forming of bulk metallic glasses: a review, JOM 68 (2016) 1246–1261.

[14] L. Thijs, F. Verhaeghe, T. Craeghs, J.V. Humbeeck, J.-P. Kruth, A study of the microstructural evolution during selective laser melting of Ti–6Al–4V, Acta Mater. 58 (2010) 3303–3312.

[15] T. Vilaro, V. Kottman-Rexerodt, M. Thomas, C. Colin, P. Bertrand, L. Thivillon, S. Abed, V. Ji, P. Aubry, P. Peyre, T. Malot, Direct fabrication of a Ti-47Al-2Cr-2Nb alloy by selective laser melting and direct metal deposition processes, Adv. Mater. Res. 89 (2010) 586–591.

[16] B. Zheng, Y. Zhou, J.E. Smugeresky, E.J. Lavernia, Processing and behavior of Fe-Based metallic glass components via laser-engineered net shaping, Metall. Mater. Trans. A 40 (2009) 1235–1245.

[17] F. Audebert, R. Colaco, R. Vilar, H. Sirkin, Production of glassy metallic layers by laser surface treatment, Scr. Mater. 48 (2003) 281–286.

[18] S. Katakam, J.Y. Hwang, S. Paital, R. Banerjee, H. Vora, N.B. Dahotre, In situ laser synthesis of Fe-Based amorphous matrix composite coating on structural steel, Metall. Mater. Trans. A 43 (2012) 4957–4966.

[19] A. Inoue, A. Takeuchi, Recent development and application products of bulk glassy alloys☆, Acta Mater. 59 (2011) 2243–2267.

[20] W.H. Wang, R.J. Wang, F.Y. Li, D.Q. Zhao, M.X. Pan, Elastic constants and their pressure dependence of Zr41Ti14Cu12.5Ni9Be22.5C1 bulk metallic glass, Appl. Phys. Lett. 74 (1999) 1803–1805.

[21] W.H. Wang, C. Dong, C.H. Shek, Bulk metallic glasses, Mater. Sci. Eng. R Rep. 44 (2004) 45–89.

[22] S. Pauly, L. Löber, R. Petters, M. Stoica, S. Scudino, U. Kühn, J. Eckert, Processing metallic glasses by selective laser melting, Mater. Today 16 (2013) 37–41.

[23] H.Y. Jung, S.J. Choi, K.G. Prashanth, M. Stoica, S. Scudino, S. Yi, U. Kühn, D.H. Kim, K.B. Kim, J. Eckert, Fabrication of Fe-based bulk metallic glass by selective laser melting: a parameter study, Mater. Des. 86 (2015) 703–708.

[24] C.D. Prest, Layer-by-layer Construction with Bulk Metallic Glasses.

[25] X.P. Li, C.W. Kang, H. Huang, L.C. Zhang, T.B. Sercombe, Selective laser melting of an Al86Ni6Y4.5Co2La1.5 metallic glass: processing, microstructure evolution and mechanical properties, Mater. Sci. Eng. A 606 (2014) 370–379.

[26] X.P. Li, C.W. Kang, H. Huang, T.B. Sercombe, The role of a low-energy–density rescan in fabricating crack-free Al85Ni5Y6Co2Fe2 bulk metallic glass composites via selective laser melting, Mater. Des. 63 (2014) 407–411.

[27] D.D. Gu, W. Meiners, K. Wissenbach, R. Poprawe, Laser additive manufacturing of metallic components: materials, processes and mechanisms, Int. Mater. Rev. 57 (2012) 133–164.

[28] X.P. Li, M.P. Roberts, S. O'Keeffe, T.B. Sercombe, Selective laser melting of Zr-based bulk metallic glasses: processing, microstructure and mechanical properties, Mater. Des. 112 (2016) 217–226.

[29] M.L. Montero Sistiaga, R. Mertens, B. Vrancken, X. Wang, B. Van Hooreweder, J.-P. Kruth, J. Van Humbeeck, Changing the alloy composition of Al7075 for better processability by selective laser melting, J. Mater. Process. Technol. 238 (2016) 437–445.

[30] A. Domashenkov, A. Borbély, I. Smurov, Structural modifications of WC/Co nanophased and conventional powders processed by selective laser melting, Mater. Manuf. Process. (2016) 1–8.

[31] H. Kakiuchi, A. Inoue, M. Onuki, Y. Takano, T. Yamaguchi, Application of Zr-Based bulk glassy alloys to golf clubs, Mater. Trans. 42 (2001) 678–681.

[32] S.R. Stock, Recent advances in X-ray microtomography applied to materials, Int. Mater. Rev. 53 (2013) 129–181.

[33] S.D. Zhang, J. Wu, W.B. Qi, J.Q. Wang, Effect of porosity defects on the long-term corrosion behaviour of Fe-based amorphous alloy coated mild steel, Corros. Sci. 110 (2016) 57–70.

[34] G. He, Z.F. Zhang, W. Löser, J. Eckert, L. Schultz, Effect of Ta on glass formation, thermal stability and mechanical properties of a Zr52.25Cu28.5Ni4.75Al9.5Ta5 bulk metallic glass, Acta Mater. 51 (2003) 2383–2395.

[35] B.A. Sun, W.H. Wang, The fracture of bulk metallic glasses, Prog. Mater. Sci. 74 (2015) 211–307.

[36] G. Yang, X. Lin, F. Liu, Q. Hu, L. Ma, J. Li, W. Huang, Laser solid forming Zr-based bulk metallic glass, Intermetallics 22 (2012) 110–115.

[37] E.V. Kharanzhevskiy, M.D. Krivilyov, Laser sintering of Fe-Ni nanocomposites, Phys. Metals Metallogr. 111 (2011) 53–61.

[38] P. Krakhmalev, I. Yadroitsev, Microstructure and properties of intermetallic composite coatings fabricated by selective laser melting of Ti–SiC powder mixtures, Intermetallics 46 (2014) 147–155.

[39] Q.S. Zhang, D.Y. Guo, A.M. Wang, H.F. Zhang, B.Z. Ding, Z.Q. Hu, Preparation of bulk Zr55Al10Ni5Cu30 metallic glass ring by centrifugal casting method, Intermetallics 10 (2002) 1197–1201.

[40] C. Qiu, C. Panwisawes, M. Ward, H.C. Basoalto, J.W. Brooks, M.M. Attallah, On the role of melt flow into the surface structure and porosity development during selective laser melting, Acta Mater. 96 (2015) 72–79.

[41] Y.F. Shen, D.D. Gu, P. Wu, Development of porous 316L stainless steel with controllable microcellular features using selective laser melting, Mater. Sci. Technol. 24 (2008) 1501–1505.

[42] Q. Jia, D. Gu, Selective laser melting additive manufactured Inconel 718 superalloy parts: high-temperature oxidation property and its mechanisms, Opt. Laser Technol. 62 (2014) 161–171.

[43] M.D. Demetriou, M.E. Launey, G. Garrett, J.P. Schramm, D.C. Hofmann, W.L. Johnson, R.O. Ritchie, A damage-tolerant glass, Nat. Mater. 10 (2011) 123–128.